

Constraints on the e^\pm pair injection of pulsar halos: Implications from the Galactic diffuse multi-TeV gamma-ray emission

Kai Yan *School of Astronomy and Space Science, Nanjing University, Nanjing 210023, China*Ruo-Yu Liu **School of Astronomy and Space Science, Nanjing University, Nanjing 210023, China
and Key laboratory of Modern Astronomy and Astrophysics (Nanjing University),
Ministry of Education, Nanjing 210023, China*

(Received 1 November 2022; accepted 24 April 2023; published 16 May 2023)

Diffuse gamma-ray emission (DGE) has been discovered over the Galactic disk in the energy range from sub-GeV to sub-PeV. While it is believed to be dominated by the pionic emission of cosmic ray hadrons via interactions with interstellar medium, unresolved gamma-ray sources may also be potential contributors. TeV gamma-ray halos around middle-aged pulsars have been proposed as such sources. Their contribution to DGE, however, highly depends on the injection rate of electrons and the injection spectral shape, which are not well determined based on current observations. The measured fluxes of DGE can thus provide constraints on the e^\pm injection of the pulsar halo population in turn. In this paper, we estimate the contribution of pulsar halos to DGE based on the Australia Telescope National Facility pulsar samples with taking into account the off-beam pulsars. The recent measurement on DGE by Tibet AS γ and an early measurement by Multiple Institution Los Alamos Gamma Ray Observatory (MILAGRO) are used to constrain the pair injection parameters of the pulsar halo population. Our result may be used to distinguish different models for pulsar halos.

DOI: [10.1103/PhysRevD.107.103028](https://doi.org/10.1103/PhysRevD.107.103028)

I. INTRODUCTION

The Galactic diffuse gamma-ray emission (DGE) is the most prominent structure in the gamma-ray sky, which appears as a bright band associated with the Galactic plane. Measurement of DGE over the entire Galactic plane from tens of MeV up to TeV energies has been done by Fermi Large Area Telescopes (Fermi-LAT) [1,2]. Ground-based detectors such as Multiple Institution Los Alamos Gamma Ray Observatory (MILAGRO) [3] and Astrophysical Radiation with Ground-based Observatory at Yangbajing (ARGO-YBJ) [4] have measured the DGE in a fraction of the Galactic plane due to their limited observable sky and extend the DGE spectrum to several TeV. More recently, the Tibet AS γ experiment [5] reported the discovery of diffuse gamma-ray emission between 100 TeV and 1 PeV in the Galactic disk for the first time.

The main component of the DGE is believed to be generated by cosmic-ray (CR) hadrons, which are mostly protons, interacting with interstellar medium (ISM). However, due to the limited sensitivity of instruments, contributions from some faint, extended sources may also

be counted in the diffuse emission, such as TeV pulsar halos, from sub-TeV band to sub-PeV band [6–10].

TeV pulsar halos are spatially extended gamma-ray emissions around middle-aged pulsars. Due to proper motions, these middle-aged pulsars have escaped their associated supernova remnants and are traversing the ISM. Energetic e^\pm pairs (hereafter we do not distinguish electrons from positrons, unless otherwise specified) that are accelerated in their pulsar wind nebulae can escape to the surrounding ISM, up-scattering the cosmic microwave background (CMB) as well as infrared radiation field in the Galaxy [11,12], forming halolike gamma-ray sources. TeV halos are firstly discovered at multi-TeV band by the High Altitude Water Cherenkov telescope around two nearby middle-aged pulsars, namely, PSR J0633 + 1746 (the Geminga pulsar) and PSR B0656 + 14 (the pulsar in the Monogem ring, also referred to as the Monogem pulsar) [13]. Recent observations of the Large High Altitude Air Shower Observatory (LHAASO) [14] identified another pulsar halos, LHAASO J0621 + 3755, with spectrum extending beyond 100 TeV.

The steep TeV gamma-ray surface brightness profiles of pulsar halos measured by the High Altitude Water Cherenkov telescope and LHAASO intuitively indicate a suppressed diffusion zone around the pulsars, although the data can be also explained with the standard interstellar diffusion

*ryliu@nju.edu.cn

coefficient under certain conditions [15,16]. Regardless of the ongoing debate on the particle transport mechanism in pulsar halos [17–19], even with the standard diffusion coefficient, i.e., $D(E) = 4 \times 10^{28} (E_e/1 \text{ GeV})^{1/3} \text{ cm}^2/\text{s}$ (e.g., [20]), high-energy electrons will cool via synchrotron and inverse Compton (IC) radiation before diffusing a distance of $r_{\text{diff}} = 2\sqrt{D(E)t_{\text{cool}}(E)} \simeq 400(E_e/100 \text{ TeV})^{-1/3} \text{ pc}$, where we consider a Galactic magnetic field of $3 \mu\text{G}$ for the synchrotron radiation loss and the CMB radiation field as the target for the IC radiation loss for the cooling timescale of electrons t_{cool} . This diffusion distance is comparable to the thickness of the Galactic disk, implying that injected high-energy electrons in pulsar halos will deposit most of their energies in the Galactic disk (for more details see Appendix A). The detailed amount of deposited energy goes into the TeV band depends on some model parameters such as the injection spectral shape and the efficiency of spindown energy of pulsars being converted to energies of electrons.

Linden and Buckman [6] assumed every young and middle-aged pulsar can power a gamma-ray halo, and they simulated a steady-state pulsar population in the Galaxy based on the supernova rate and the distribution of massive stars, pulsars, and supernova remnants. By assigning an initial rotation period and magnetic field to each generated pulsar following the study of the observed pulsar population, they showed that the injected electrons from pulsars can dominate the DGE at the TeV band and explain MILAGRO data given appropriate choice of the electron injection spectrum. While the true DGE fraction contributed by pulsar halos highly depends on the properties of electron injections, the observed DGE can be conservatively regarded as an upper limit of the gamma-ray emission from the pulsar halo population, which then can be used to constrain electron injection in pulsar halos.

In this study, we aim to explore the constraints on the electron injection of pulsar halos based on the DGE measured by AS γ [5] and MILAGRO [3]. Different from previous studies, we will employ observed pulsar population based on the Australia Telescope National Facility (ATNF) pulsar catalog [21] instead of a simulated pulsar population. This is to reduce the possible deviation of the simulation from reality. In addition, using the observed pulsar sample would allow us to predict the contribution from each realistic pulsar. On the other hand, another difference from Linden and Buckman [6] will be the exclusion of relatively young pulsars with age less than 100 kyr in our calculation. Electrons accelerated in those compact young pulsar wind nebula (PWNe) may be well confined and have not escaped to ISM. They have been likely resolved by many TeV gamma-ray instruments and are removed in the DGE analysis by AS γ for instance. Exclusion of those relatively young pulsars will make our constraints more conservative.

This rest of the paper is organized as follows. In Sec. II, we introduce the method to select the pulsar samples and to calculate their contribution to the DGE. In Sec. III, we show

the main results of this work. In Sec. IV, we further discuss some model uncertainties. In Sec. V, we present our conclusion.

II. METHOD

A. Sample selection

There are more than 3000 pulsars recorded in the ATNF catalog. We select pulsars from the ATNF catalog with the following three conditions:

- (1) with characteristic age between 100 kyr and 10 Myr;
- (2) within the region of interest (ROI) for AS γ (i.e., $25^\circ < l < 100^\circ$, $|b| < 5^\circ$) and for MILAGRO (i.e., $40^\circ < l < 100^\circ$, $|b| < 5^\circ$);
- (3) more than 0.5 degree away from the observed TeV sources in the TeVcat [22].

The first condition is to exclude the contribution of relatively young pulsars and millisecond pulsars. For those relatively young pulsars, the injected electrons may mainly radiate in their PWNe and do not form pulsar halos. There also exists a population of old pulsars which have been spun up through accretion of matter from a donor star in a close binary system, i.e., the millisecond pulsars. They may have quite complex ambient environments than middle-aged pulsars. Although TeV pulsar halos might also exist around millisecond pulsars [23], we ignore their possible contribution in this work to be on the conservative side. The third condition mainly follows the treatment of AS γ in their analysis of DGE [5], where they masked a region of 0.5° radius centered at each source recorded in the TeVcat in order to exclude contributions of pulsars therein. Note that many TeV sources had not been discovered yet in the era of MILAGRO, and hence the measurement of MILAGRO on DGE should contain a lot of contributions from bright TeV sources which are excluded in the measurement of AS γ . For simplicity, however, we still perform the masking procedure when comparing with MILAGRO data, since this would only lead to more conservative constraints.

Among all the pulsars samples, PSR J1952 + 3252 is of an extremely high spin-down luminosity of $3.7 \times 10^{36} \text{ erg s}^{-1}$, which is two orders higher than that of Geminga pulsar, while its distance from Earth is about 3 kpc. Regardless of the positive theoretical prediction [24], no TeV gamma-ray emission has been detected from the pulsar or its associated PWN yet. Actually, the pulsar is still located inside a supernova remnant (i.e., CTB 80) implying that it probably has not reached the middle-age stage. This possibility is corroborated by its fast spin with a rotation period of only 40 ms. Unless the initial rotation period is far less than this value, its true age may be considerably shorter than its characteristic age (i.e., 107 kyr). We speculate that the accelerated electrons are still confined inside its SNR-PWN complex, and their IC radiation may be suppressed due to a high magnetic field therein. Therefore, we exclude this specific pulsar from our samples. All the pulsar samples

selected in our calculation are listed in Appendix B (see Table I).

B. Modeling the gamma-ray flux of pulsar halos

For a single pulsar halo, the energy losses of electrons through a combination of synchrotron radiation and IC radiation can be given by

$$\frac{dE_e}{dt} = -\frac{4}{3}\sigma_T c \left(\frac{E_e}{m_e c^2}\right)^2 \left[U_B + \sum_i U_i / \left(1 + 4\frac{E_e \epsilon_i}{m_e^2 c^4}\right)^{3/2} \right], \quad (1)$$

where σ_T is the Thompson cross section. The magnetic field strength is taken as $3 \mu\text{G}$ and the magnetic energy density U_B is 0.22 eV cm^{-3} . U_i and ϵ_i represent the energy density and the typical photon energy of the i th component of the interstellar radiation field assuming a black body or a gray body distribution with temperature T_i for their spectra (i.e., $\epsilon_i = 2.82kT_i$). The considered target radiation field includes the CMB radiation field ($T_{\text{CMB}} = 2.73 \text{ K}$ and $U_{\text{CMB}} = 0.26 \text{ eV cm}^{-3}$), a far-infrared radiation field ($T_{\text{FIR}} = 30 \text{ K}$ and $U_{\text{FIR}} = 0.3 \text{ eV cm}^{-3}$), and a visible light radiation field ($T_{\text{VIS}} = 5000 \text{ K}$, $U_{\text{VIS}} = 0.3 \text{ eV cm}^{-3}$). The injected electron spectrum following a power-law with an exponential cutoff, denoted as

$$Q(E_e, t) = N_0(t) E_e^{-s} e^{-E_e/E_{\text{max}}}, \quad (2)$$

where s is the spectral index and E_{max} is the cutoff energy. Assuming the spin-down energy loss is totally governed by the dipole radiation, i.e., under the condition of braking index $n = 3$, the normalization constant N_0 can be determined by

$$\int_{E_0}^{\infty} E_e Q(E_e, t) dE_e = \eta_e L_{s,j}(t) = \eta_e \frac{L_{0,j}}{(1 + t/\tau_{0,j})^2}, \quad (3)$$

where η_e represents the fraction of the pulsar spin-down energy that goes into the electrons, which is another important input parameter. Here L_s is the spin-down luminosity of the pulsar, L_0 is the initial spin-down luminosity, and τ_0 is the initial spin-down timescale. The subscript j represents the j th pulsar within the ROI, as listed in Table I. The minimum integral energy E_0 here is set to be 50 GeV . The age of the pulsar $t_{\text{age},j}$, characteristic age $\tau_{c,j}$, and initial spin-down timescale $\tau_{0,j}$ are related by

$$t_{\text{age},j} = \tau_{c,j} - \tau_{0,j} = \frac{P_j}{2\dot{P}_j} \left[1 - \left(\frac{P_{0,j}}{P_j} \right)^2 \right] \quad (4)$$

in which $P_{0,j}$ is the initial rotation period, P_j is the current rotation period, and \dot{P}_j is the period derivative. The electrons differential number density at the present time (i.e., $t = t_{\text{age},j}$) for j th pulsar halo is calculated by

$$N_j(E_e) = \int_0^{t_{\text{age},j}} Q(E_e, t) dt \frac{dE_g}{dE_e}, \quad (5)$$

where the relationship between initial injected energy E_g and current energy E_e can be obtained from Eq. (1). After obtaining $N_j(E_e, t_{\text{age},j})$, we calculate the IC and synchrotron luminosity $L_j(E_\gamma)$ of the j th pulsar halo according to the semianalytical method given by Khangulyan *et al.* [25] and Fouka and Ouichaoui [26], respectively.

To get the total intensity of unresolved pulsar halos, we sum over the contribution of each single pulsar halo. Note that there should exist many pulsars the lighthouse-like radiation beam of which do not sweep Earth as they spin. As a result, we cannot detect them but they may still inject electrons in the surrounding ISM and form pulsar halos. The fraction of those off-beamed pulsars depend on the size of the beam. Taking into account of pulsar halos from off-beamed pulsars, we weight the contribution of each single pulsar halo by its beaming fraction. It leads to an average intensity

$$I_\gamma = \frac{1}{\Omega} \sum_j \frac{L_j(E_\gamma)}{4\pi d_j^2 f_{\text{beam},j}}, \quad (6)$$

where $f_{\text{beam},j}$ represents the ratio of the solid angle subtended by the radiation beam (which may be related to the magnetic inclination solid angles) of a pulsar to 4π . Following the study in Ref. [27], we adopt $f_{\text{beam},j} = 0.011[\log(\tau_{c,j}/100)]^2 + 0.15$ and $\tau_{c,j}$ in unit of Myr. Ω is the corresponding solid angle of the ROI after masking the known TeV sources, which are 0.219 and 0.177 sr , respectively, for AS γ and MILAGRO.

C. Influence of model parameters

Before we present our main results, we show the influence of some model parameters that would be helpful to understand the results. The first one is the initial rotation period P_0 . P_0 can be derived based on the assumed spindown history of the pulsar if the true age of the pulsar is known. However, the true ages of most pulsars are unknown and hence we can only make assumptions for P_0 . Its value has an enormous influence on the early injection history of electrons. The smaller P_0 is, the higher initial spindown luminosity the pulsar will get. Therefore, a vast amount of electrons would be injected at an early time if a small P_0 is assumed. Given the assumed magnetic field and the radiation field, electrons with energy $> 10 \text{ TeV}$ would cool at 100 kyr . As a result, we would expect electrons injected at early time with energy lower than 10 TeV are accumulated to the present time and cause a huge flux below $\sim \text{TeV}$. As illustrated in the left panel of Fig. 1, we show the influence of initial periods on the resultant gamma-ray spectrum. We see the strong dependency on P_0 at $\lesssim \text{TeV}$ energy, but the spectrum is almost unaffected above several TeV.

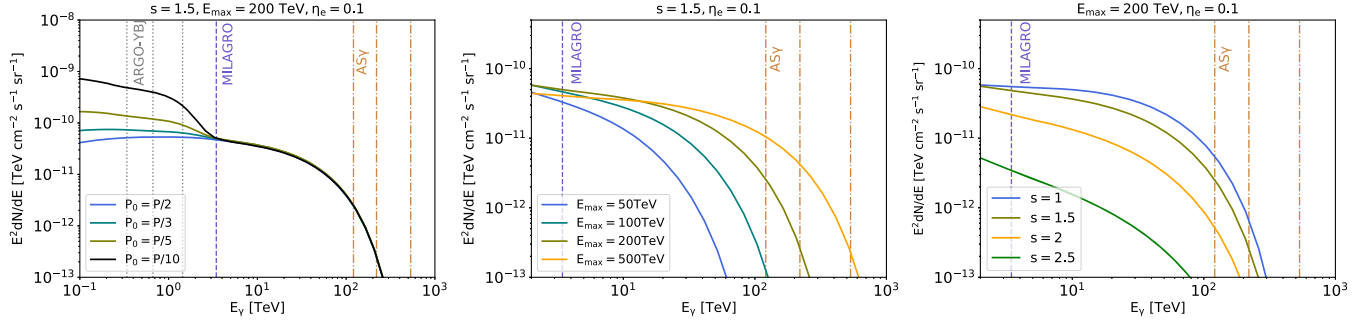


FIG. 1. Spectral energy distribution (SED) of the population of unresolved pulsar halos within $25^\circ < l < 100^\circ$, $|b| < 5^\circ$. The left panel shows the influence of initial period models on the SED. The middle panel shows the influence of cutoff energy E_{\max} on the SED, and the right panel shows that of spectral index s . Dashed lines show the observational energies of instruments.

On the other hand, it should be noted that the electromagnetic environment where injected electrons reside could be very different from that of ISM at the early evolutionary stage of the PWN. The magnetic field strength in some young PWNe are found to be much higher than that of the interstellar magnetic field (e.g., [28–35]), electrons injected at early time, which are very likely well confined in the PWN, may cool very efficiently. Also, the expansion of PWN at early time may lead to adiabatic cooling of confined electrons. As a result, these relatively low-energy electrons may not survive at the present time and hence do not produce the GeV–TeV bump as shown in the left panel of Fig. 1. Given such a large uncertainty, we only use the MILAGRO data and the ASy data, which are above several TeV, to constrain the parameters in the following sections and ignore the DGE measured by ARGON-YBJ intentionally.

It is straightforward to envisage that the cutoff energy E_{\max} and the spectral index s in the injection electron spectrum are important to the resultant diffuse gamma-ray flux. In the middle and right panels of Fig. 1, we compare the resultant gamma-ray spectra with different cutoff energies and injection spectral indexes, respectively, while keeping the total injection luminosity the same. E_{\max} and s both affect the gamma-ray spectral shape but do not alter the level of the peak flux significantly. On the contrary, the conversion efficiency η_e , which is proportional to the injection luminosity, can lead to a systematic shift in the amplitude of the gamma-ray flux without changing the spectral shape, which is not illustrated here. As expected, a larger cutoff energy and a harder injection spectrum result in a higher flux at high energy end, and vice versa. Thus, we may expect that the MILAGRO measurement at several TeV and the ASy measurement at sub-PeV would play different roles in constraining injection parameters.

III. RESULTS

In this section, we show the constraints on the electron injection under different sets of model parameters. As mentioned before, the diffuse gamma-ray fluxes measured by ASy and MILAGRO should contain the contribution

from both the pionic emission induced by cosmic-ray hadrons and unresolved sources. We adopt the factorized model developed by Ref. [36] to estimate a conservative contribution of the cosmic-ray hadronic component. We then calculate the corresponding IC fluxes under a set of injection parameters from the pulsar halo population, and find out the critical combinations of parameters with which the sum of the hadronic component and the IC component reach the 68.3% (or 99.7%) upper limit of any data point measured by either ASy or MILAGRO. The corresponding parameter set is then regarded as the constraints on the electron injection parameters. In Fig. 2, we show for instance a few cases that IC emission of pulsar halos and pionic emission of CR hadrons reach the 68.3% upper limits of DGE observed by ASy or MILAGRO under different combination of parameters.

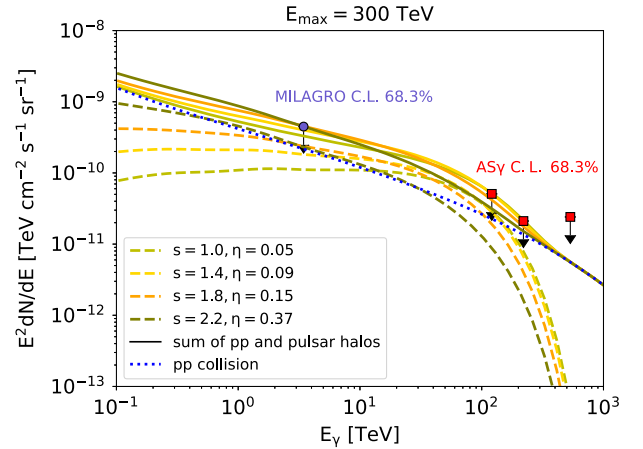


FIG. 2. Expected contribution of unresolved pulsar halos to DGE under different parameter sets. The purple circle marks the 68.3% upper limit of photon fluxes observed by MILAGRO, and red squares mark 68.3% upper limits of ASy. The blue dotted curve shows the flux of pp collisions by cosmic-ray hadrons. Dashed curves with different colors show the contribution of unresolved pulsar halos with different sets of parameters as labeled in the figure. Solid curves show the total diffuse gamma-ray fluxes of pp collisions and unresolved pulsar halos.

A. Baseline model setups

For the sake of simplicity and to be in accordance with the previous modeling setups (e.g., [13,14,37,38]), we first consider E_{\max} as a common parameter over all pulsar halos. We then explore constraints on the conversion efficiency η_e for different E_{\max} or spectral index s . We present the result in Fig. 3, where the left panel shows the two-dimensional constraints between E_{\max} and η_e , with s fixed to 1.5 as the benchmark value. The right panel shows constraints on the combination of s and η_e , with E_{\max} fixed to 300 TeV as the benchmark value. Solid and dashed curves represent constraints from AS γ ($25^\circ < l < 100^\circ$, $|b| < 5^\circ$) and MILAGRO ($40^\circ < l < 100^\circ$, $|b| < 5^\circ$), respectively. Black and blue curves show the combination of parameters that reach the 99.7% and 68.3% upper limits of photon flux, respectively. Parameters space shaded with cyan and blue are the allowed region corresponding to the 99.7% and 68.3% upper limits, respectively.

We see that the upper limits of η_e obtained from AS γ depend heavily on E_{\max} , as illustrated in solid lines in Fig. 3(a). This is because the injected electron flux at the energy relevant with the energy band of AS γ , i.e., several hundred of TeV, are very sensitive to the value of E_{\max} . The resulting gamma-ray fluxes above 100 TeV have drastic changes when E_{\max} increases from 50 to 500 TeV, as shown in Fig. 1(a). On the other hand, in the energy band of MILAGRO, the photon fluxes and upper limits of η_e are much less dependent by E_{\max} unless E_{\max} drops below 20 TeV. For a fixed E_{\max} , the upper limit of η_e monotonically increases with the injection spectral index s based on either the AS γ data or the MILAGRO data, as shown in Fig. 1(b). Combining the two panels, we may conclude that the 68.3% upper limits of η_e can be constrained to be $\lesssim 0.1$ for $s < 1.8$. This is a relatively strong parameter restriction,

considering 0.1 is a commonly taken value in literature (e.g., [6]). For $s > 2$, both AS γ and MILAGRO data give weak constraints on η_e , since the resulting gamma-ray fluxes peak at lower energy ranges. However, as we mentioned earlier, the DGE data at lower energies does not help because of the large uncertainty in theoretical prediction.

B. E_{\max} as a function of spin-down luminosity

The cutoff energy E_{\max} is considered to be the same for all pulsars in the previous section. In reality, E_{\max} may vary from pulsar to pulsar, depending on their properties. It has been suggested [39–41] that the maximum achievable energy of electrons in a PWN depends on the maximum potential drop between the pulsar and infinity. Based on the *Hillas* criterion, the maximum energy can be given by $E_{\max} = eB_{\text{TS}}R_{\text{TS}}$ regardless of the acceleration mechanism, where B_{TS} and R_{TS} are the magnetic field and size of the termination shock, respectively. Denoting the ratio of the magnetic energy to the pulsar wind energy by η_B , we have $B_{\text{TS}}^2/8\pi = \eta_B L_s/(4\pi R_{\text{TS}}^2 c)$. The magnetic field at the termination shock B_{TS} can be estimated as $B_{\text{TS}} = (2\eta_B)^{1/2} R_{\text{TS}}^{-1} (L_s/c)^{1/2}$ then. As a result,

$$E_{\max} = (2\eta_B)^{1/2} e(L_s/c)^{1/2}, \quad (7)$$

which is expressed as a fraction of $(2\eta_B)^{1/2}$ of the pulsar potential drop $\Phi_{\text{PSR}} = e(L_s/c)^{1/2}$. We may find that $\eta_B \approx 0.2(E_{\max}/100 \text{ TeV})^2 (L_s/10^{34} \text{ erg s}^{-1})^{-1}$ based on Eq. (7). Previous studies have shown that $E_{\max} \gtrsim 100 \text{ TeV}$ is needed to model the spectra of the observed pulsar halos (e.g., $E_{\max} = 150 \text{ TeV}$ for LHAASO J0621 + 3755 [14]),

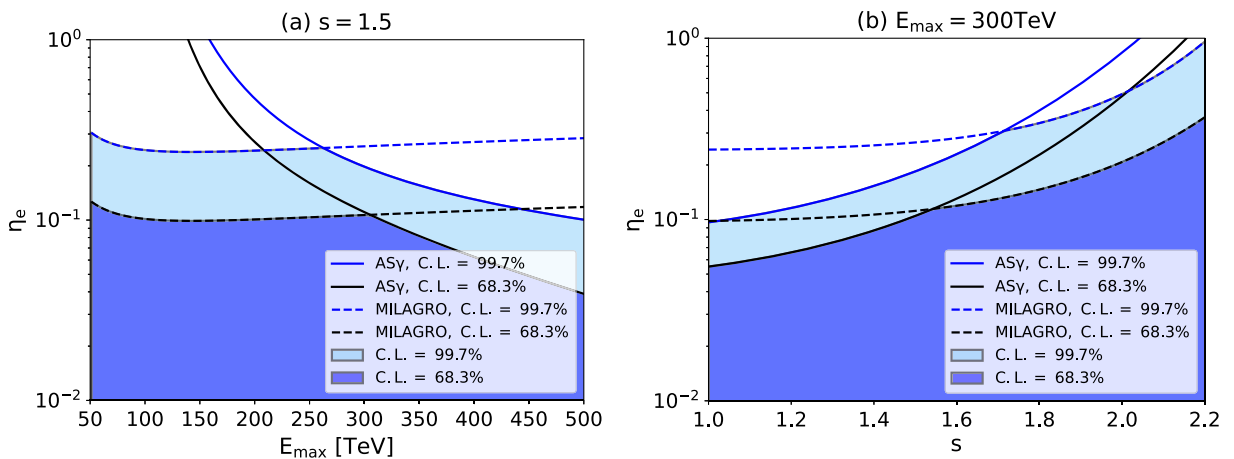


FIG. 3. (a) Two-dimensional constraints between E_{\max} and η_e , with s fixed to 1.5 (b) two-dimensional constraints between s and η_e , with E_{\max} fixed to 300 TeV. Black and blue curves show the boundary of injection parameters that reach 68.3% confidence level and 99.7% confidence level of flux, respectively. Solid and dashed curves represent cases for AS γ and MILAGRO, respectively. The left panel shows the constraints of combination of E_{\max} and η_e , with s fixed. And the right panel shows the constraints of combination of s and η_e , with E_{\max} fixed.

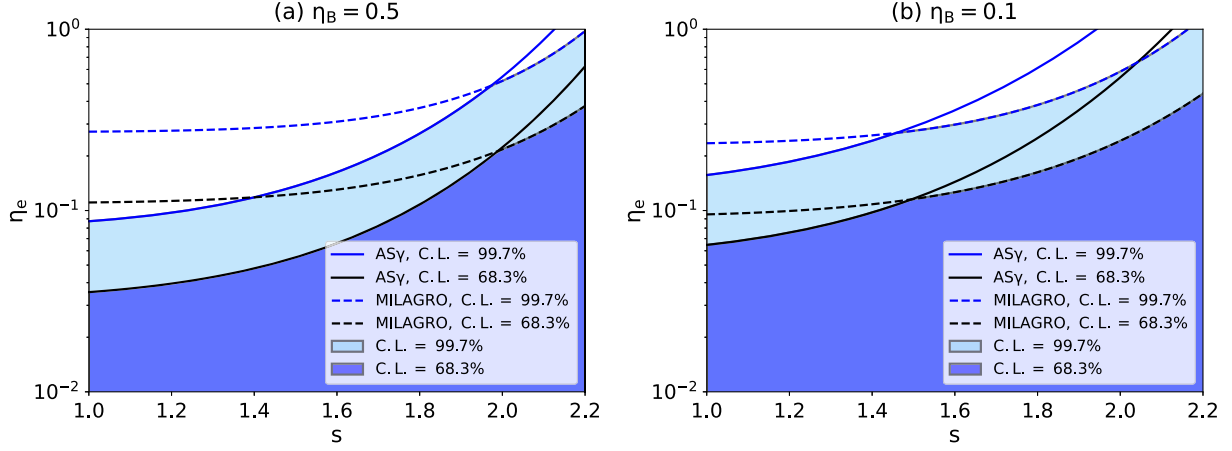


FIG. 4. Two-dimensional constraints between s and η_e , with E_{\max} computed from Eq. (7) with (a) $\eta_B = 0.5$ and (b) $\eta_B = 0.1$. The meaning of graphical elements is the same as in Fig. 3.

which implies that η_B should not be smaller than 0.1 for middle-aged pulsar halos.

In Fig. 4, we present the two-dimensional constraints between s and η_e , with E_{\max} computed from Eq. (7). In the left panel, we set $\eta_B = 0.5$ as an optimistic case, while we set $\eta_B = 0.1$ in the right panel as a conservative case. As expected, we see that the constraints obtained from MILAGRO, i.e., dashed lines, have no significant changes compared with those shown in Fig. 3(b), because of the yielded gamma-ray flux at several TeV does not depend on E_{\max} much. On the contrary, the constraints obtained from AS γ (solid lines) vary remarkably with changing η_B . In general, the case of $\eta_B = 0.1$ yields a more or less comparable constraint on η_e and s to that with a fixed $E_{\max} = 300$ TeV. However, it may be worth noting that employing Eq. (7) will increase the contribution from more energetic pulsars while decrease the contribution from less energetic pulsars at the energy band of AS γ . For $\eta_B = 0.1$, only those pulsars with $L_s \gtrsim 2 \times 10^{34}$ erg/s may generate electrons above 100 TeV. As a result, the resulting gamma-ray flux above 100 TeV are dominated by a few pulsar halos with the most energetic pulsars. The constraint on the parameters would be less robust in this case since it would be easily influenced by the properties of some most energetic pulsars in the sample.

C. Broken power-law spectrum

In the previous calculation, we adopt a single power-law injection spectrum with a high-energy exponential cutoff. For relatively soft injection spectra, i.e., $s > 2$, the obtained constraints on parameters are quite relaxed. This is because in the cases of $s > 2$, the resulting IC flux is mainly concentrated at the GeV band. Some previous literature (e.g., [42,43]) considered a broken power-law form for the injection electron spectrum with the break energy E_b usually at 0.1–1 TeV. Below the break energy, the spectrum is very hard, which is roughly equivalent to setting the

minimum energy E_0 to E_b . As a result, introducing a spectral break in the case of $s > 2$ will increase the energies distributed at the high-energy end provided the same total injection luminosity. We then adopt a broken power-law injection spectrum, i.e.,

$$Q(E_e, t) = N_0(t) \times e^{-E_e/E_{\max}} \times \begin{cases} (E_e/E_b)^{-s_1} & \text{for } E_e \leq E_b \\ (E_e/E_b)^{-s_2} & \text{for } E_e > E_b \end{cases}, \quad (8)$$

with $s_2 \geq 2$, and repeat the calculation mentioned above.

In Fig. 5, we present the result in this case. The low energy spectral index is fixed to $s_1 = 1.5$ and E_{\max} is computed from Eq. (7) with $\eta_B = 0.5$. In the left panel, we fix the high energy spectral index $s_2 = 2.2$ and explore the effects of E_b , while we fix $E_b = 1$ TeV and vary s_2 in the right panel. We see that the MILAGRO data is more constraining than AS γ data in the considered parameter space. The constraint is stricter than that in the single power-law case. In general, we can rule out a very large value of η_e (~ 1) unless the injection spectrum is very soft at high energies, i.e., $s_2 > 2.4$ and $E_b < 0.2$ TeV.

D. Comparison with observed pulsar halos

The results obtained in previous sections represent a general constraint on the particle injection from the pulsar halo population. It may be worth comparing the constraint with the parameters obtained by fitting individual pulsar halos, namely, the halos of the Geminga pulsar, the Monogem pulsar and PSR J0622 + 3749. For the former two halos, the measured spectra have large uncertainties and hence the particle injection parameters are not well constrained. Taking the Geminga pulsar as an example, the observed spectrum of its TeV gamma-ray halo can be interpreted with various combinations of s and η_e . According to previous literature, the injection spectrum could be as hard as $s = 1.5$ – 1.6 with $\eta_e = 0.03$ – 0.05 [15,16] or as soft as

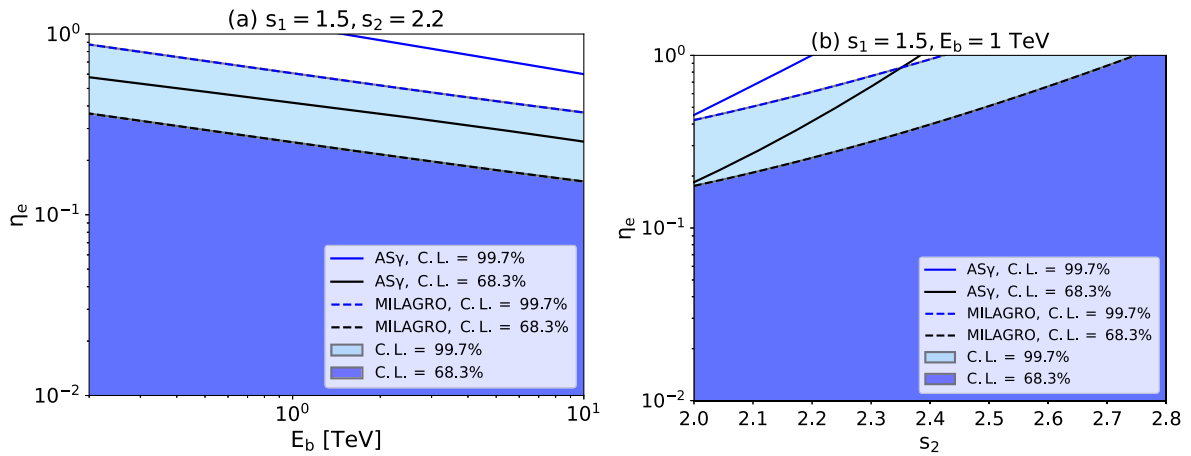


FIG. 5. (a) Two-dimensional constraints between E_b and η_e , with s_1 fixed to 1.5 and s_2 fixed to 2.2. (b) Two-dimensional constraints between s_2 and η_e , with s_1 fixed to 1.5 and E_b fixed to 1 TeV. The meaning of graphical elements is the same as in Fig. 3.

$s = 2.3$ – 2.4 with $\eta_e = 0.4$ – 0.6 [38,43] under the pure diffusion model, which is consistent with the 68.3% C.L. upper limit as shown in Figs. 3 and 4. The fitting to the Monogem’s halo results in similar parameters. On the other hand, for the halo of PSR J0622 + 3749, the measurements of LHAASO and Fermi-LAT suggest a hard injection spectrum of $s = 1.5$ with a high pair conversion efficiency $\eta_e = 0.4$ [14], which exceeds the constraint from the upper limit (UL) of 99.7% C.L. of the DGE. However, we note that the distance of PSR J0622 + 3749 is of large uncertainty. The obtained high pair conversion efficiency is based on a “pseudodistance” of $d = 1.6$ kpc derived from the empirical relation between the gamma-ray luminosity and the spin-down luminosity for gamma-ray pulsars [44]. Provided a smaller distance of the pulsar, the requirement on the pair conversion efficiency would be less stringent since $\eta_e \propto d^2$.

On the other hand, under the model suggested by Recchia *et al.* [16], where the standard ISM diffusion coefficient is employed with considering ballistic propagation of injected pairs at small radii, the required pair conversion efficiencies for the halo of Geminga exceeds unity while for the halos of Monogem and J0622 + 3749 are around unity, even with a hard injection spectrum $s = 1.5$. With the parameters, the expected diffuse gamma-ray flux from the entire pulsar halo population would largely overshoot the measurements by MILAGRO and AS γ , which thus disfavor the model. Otherwise, one might instead argue that only a small fraction of middle-aged pulsars can form pulsar halos around them under this model, but this would raise new questions to be elucidated, such as the special conditions of forming gamma-ray halos for these pulsars.

IV. DISCUSSION

A. Possible improvements to get tighter constraints

The obtained parameter constraints are upper limits rather than exact values. To avoid introducing extra

uncertainties, we have simplified some conditions intentionally and obtained conservative upper limits. In other words, one might obtain tighter constraints after carefully considering these effects.

The instrumental detection threshold leads to a missing population of pulsars. Most pulsars are detected in the radio band, while the spin-down luminosity of pulsars do not clearly correlate with the radio luminosity. Therefore, it is possible that some pulsars of relatively high spin-down luminosity are not observable. Taking into account halos of these miss pulsars would lead to a higher expected diffuse gamma-ray flux, which can be translated into stronger constraints on injection parameters.

Yusifov and Küçük [45] derived the correction factor of the intrinsic the pulsar spatial distribution in the Galaxy based on 1400 ATNF pulsar samples at the time. Applying for their correction factor in our calculation (see Appendix C for details) leads to almost tenfold higher diffuse gamma-ray flux, and, as a consequence, the obtained upper limit of η_e would be decreased by about an order of magnitude for any given spectral index s or E_{\max} , as illustrated in Fig. 8. However, the instrumental detectivity of pulsars at nowadays must be advanced with respect to that at the time of Yusifov and Küçük [45], because of improvement of sensitivity of new radio telescopes and increase of exposure time for recent 20 years. As a result, the amount of subthreshold pulsars is very likely overestimated by employing the correction factor obtained almost 20 years ago to the pulsar sample at the present time (i.e., some of subthreshold pulsars at that time would have already been discovered today). Hence, the obtained upper limits for η_e in Fig. 8 would be too radical to be realistic after employing their correction factor. A dedicated study is needed to obtain an accurate correction factor based on the present pulsar sample, which is, however, beyond the scope of this work. In order to make our result and conclusion on the safe side, we choose not to count in the contribution of those subthreshold pulsars in the present study, noting that our conservative result can

provide nontrivial constraints on models of pulsar halos as shown in the previous section.

B. Uncertainties of the method

As mentioned at the beginning of Sec. III, we employed the factorized model proposed by Lipari and Vernetto [36] to estimate the DGE from interactions between CR hadrons and the ISM, which yields a conservative estimate of the DGE flux in the ROI ($l = 25^\circ\text{--}100^\circ$, $|b| \leq 5^\circ$) compared to the other model proposed in Lipari and Vernetto [36]. The other one, coined as the “nonfactorized” model, takes into account the hardening of CR spectra toward the inner Galactic region as inferred from the DGE measurement by Fermi-LAT [46,47]. The nonfactorized model predicts a higher CR-induced DGE flux in TeV-PeV than the factorized model by a factor of $\lesssim 2$ in the ROI. If we employ the nonfactorized model instead, the room left for the contribution of pulsar halos will be smaller, and, as a consequence, tighter constraints of injection parameters could be obtained. It may be worth noting that the CR-induced DGE flux predicted by the nonfactorized model already exceeds the 68.3% UL of the flux in energy bin of 158–398 TeV measured by AS γ . If we ignore this energy bin, then the obtained upper limits of η_e based on data in other energy bins are roughly a factor of 4 lower than those obtained with the factorized model given the same value of s .

Compared to previous studies that simulated a sample of pulsar halos based on the supernova rate, our method relies on the observed pulsars and the beam fraction of pulsars to estimate the contribution of a complete sample of pulsar halos in our Galaxy. Our calculation is based on the relation between the characteristic age and the beam fraction suggested by Ref. [27], which was obtained through the distribution of inclination of the magnetic axes of pulsars. The authors also suggested a relation between the rotation period and the beam fraction, which reads $f_{\text{beam}} = 0.09[\log(P/10 \text{ s})]^2 + 0.03$. Using the latter relation instead would lead to a slight difference (within a factor of 1.5) in the obtained upper limits of η_e as shown in Figs. 3–5, which will not influence our conclusion. On the other hand, we note that both relations lead to a mean beaming fraction of $\lesssim 0.2$ for the employed middle-aged pulsar sample, implying that the majority of middle-aged pulsars are invisible to us. Therefore, it might be an issue whether or not the properties of observed pulsars can be a good proxy for the entire pulsar population, and thus they might introduce corresponding uncertainty to our results.

Another uncertainty may come from the particle transport model. In the DGE paper of the AS γ collaboration, they masked the region within 0.5 degree of all the known TeV sources in order to get rid of the emission of sources [5]. To compare with the measurement of AS γ , we remove a pulsar from our sample if the pulsar is located within 0.5 degrees of any known TeV source. However, if the diffusion coefficient in the pulsar halo is not suppressed

as suggested by Recchia *et al.* [16], the angular size of the pulsar halo would be quite large. For example, the cooling timescale of 100 TeV electrons in 3 μG magnetic field and CMB is about 10 kyr. The diffusion coefficient would be $\sim 10^{30} \text{ cm}^2/\text{s}$ for 100 TeV electron in ISM without suppression. It leads to a diffusion distance (i.e., halo size) of $\sim 100 \text{ pc}$, or an angular size of $2^\circ (d/3 \text{ kpc})^{-1}$, where d is the distance of the pulsar. Since the halo size could be larger than 0.5° , the halos of the pulsars in the masked region could still contribute to the DGE (see details in Appendix A), especially for those nearby pulsars. In this sense, we may have underestimated the DGE flux by simply ignoring those pulsars in the masked region. To accurately estimate the flux of these pulsar halos contributed to DGE, a more sophisticated modelling is needed, e.g., considering the position of each pulsar in the Galaxy and the three-dimensional distribution of injected pairs. We leave such a study in the future work, noting that the current treatments lead to conservative constraints.

C. Constraints from the CR positron flux

In addition to DGE, cosmic-ray positron flux might be an alternative observable quantity to constrain injection parameters of pulsar halos, especially in the case of soft injection spectrum. Some previous studies have investigated the expectation of positron flux from middle-aged pulsars [43,48,49]. However, we note that the expected positron flux at Earth is highly dependent on the transport mechanism of particles in pulsar halos. Besides, the positron excess appears at sub-TeV energies, at which positrons injected at an early time of a middle-aged pulsar have not been cooled in typical interstellar magnetic field at present time and could make contribution to the positron flux at Earth. On the other hand, the amount of these early injected positrons highly depend on the initial rotation period of the pulsar P_0 (which determines the initial spindown luminosity) and the electromagnetic environment of the PWN, either of which are unknown. Thus the predicted positron flux at sub-TeV energies could have large uncertainties, preventing us from drawing a concrete conclusion. This is similar to the reason why we do not use the DGE measured by ARGO to constrain models, as illustrated in the left panel of Fig. 1.

V. SUMMARY AND CONCLUSION

Detection of TeV pulsar halos around middle-aged pulsars suggests escaping of energetic electrons from PWNe of these middle-aged pulsars. It backs up the idea that middle-aged pulsars may be important sources of cosmic-ray leptons, especially for positrons. Therefore, the gamma-ray flux of pulsar halos can reveal the properties of pair injection from the PWNe, as well as the transport mechanism of particles in ISM. If each middle-aged pulsar can form a TeV halo, then most of them are not sufficiently bright to be resolved by current instruments and hence their

emission may be counted as diffuse gamma-ray emission in the Galactic plane.

In this work, we tried to acquire constraints on the pair injection parameters of pulsar halos by the DGE flux measured by AS γ and MILAGRO. We first selected a sample of middle-aged pulsars within the ROI of AS γ and MILAGRO, excluding those pulsars located within 0.5° of known TeV sources. We then calculated the expected diffuse gamma-ray emission generated by escaping electrons from these pulsars under a set of injection parameters. We also estimated diffuse gamma-ray flux from the pionic emission of cosmic-ray hadrons, based on the ‘‘factorized’’ model developed by Ref. [36], which likely yields a conservative estimation of the pionic component. We then considered the measured DGE as upper limits of gamma-ray fluxes generated by the sum of cosmic-ray hadrons and unresolved pulsar halos. By comparing the measurements with theoretical predictions, we obtained the constraint on injection parameters of the pulsar halos such as the pair conversion efficiency η_e , the injection spectral index s and the maximum cutoff energy E_{\max} of injected electrons. More specifically, under a moderate assumption of E_{\max} , the 68.3% upper limit of DGE data gives $\eta_e \lesssim 0.1$ for $s < 1.8$. For a softer spectrum (i.e., a larger s), the MILAGRO data at several TeV energies becomes more constraining, but the overall constraints become less stringent. For $s = 2.2$, the upper limit of η_e increases to 0.4. In the case that a hardening appears in the injection spectrum below sub-TeV to a few TeV, a stricter constraint on η_e can be obtained given the same spectrum at the high-energy end.

Based on our results, we may draw the following conclusions:

- (1) The expected diffuse gamma-ray emission from unresolved pulsar halos may saturate the measured DGE flux above several TeV with reasonable parameters. Therefore, unresolved pulsar halos may likely contribute a non-negligible fraction of the measured DGE, which is consistent with the result of Ref. [6].

- (2) The large value of the pair conversion efficiency $\eta_e \sim 1$ can be generally excluded unless the injection spectrum is very soft. Our result disfavors the isotropic, unsuppressed diffusion model [16], which requires a hard injection spectrum and a large conversion efficiency $\eta_e \sim 1$.
- (3) We reiterate that the obtained constraints are generally in the conservative side because of our intentional choice of some steps in the calculation. However, some uncertainties such as the pulsar’s beam fraction might nevertheless influence the results. The future measurement of LHAASO on DGE may give more precise constraints.

ACKNOWLEDGMENTS

We thank anonymous referees for constructive reports which improve the quality of the paper. This work is supported by NSFC under Grant No. 2031105.

APPENDIX A: FRACTION OF THE HALO FLUX WITH AN UNSUPPRESSED DIFFUSION COEFFICIENT

When considering the ballistic propagation of particles at small radii (i.e., $r < 3D/c$, see Ref. [16]) with the standard ISM diffusion coefficient, i.e., $D(E) = 4 \times 10^{28} (E/1 \text{ GeV})^{1/3} \text{ cm}^2/\text{s}$, the halo size would become quite extended. We calculate the surface brightness profile of a pulsar halo in the unsuppressed diffusion scenario following Ref. [16]. In Fig. 6 we plot the fraction of the halo flux contained within 0.5° (left) and 5° (right) from a pulsar, at 10 TeV (blue curve) and 100 TeV (orange curve), as a function of the pulsar’s distance from Earth in this scenario. It can be seen that more than 50% of the halo’s emission at 10 TeV (100 TeV) would be beyond 0.5° if the pulsar is located within 2 kpc (4 kpc) from Earth. Therefore, simply removing the pulsar within 0.5° of any known TeV sources from the sample may lead to an

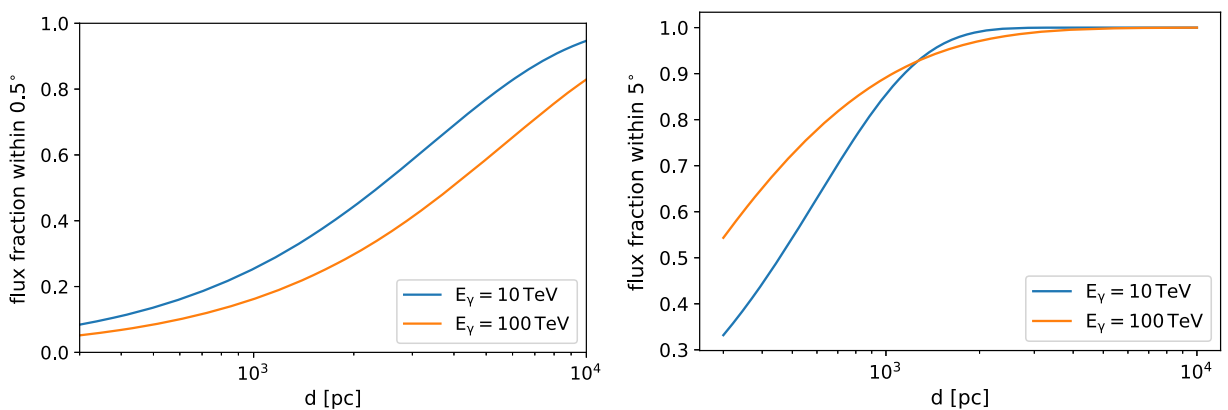


FIG. 6. Left: flux fraction of a pulsar halo within 0.5° from the pulsar as a function of the pulsar’s distance. The diffusion coefficient is assumed to be $4 \times 10^{28} (E/1 \text{ GeV})^{1/3} \text{ cm}^2/\text{s}$. The magnetic field and the radiation field are the same as mentioned in Sec. II B. Right: same as the left panel but for the flux fraction within 5° from the pulsar.

underestimation of the DGE under the unsuppressed diffusion scenario by a factor of a few. On the other hand, less than 10% of the halo's emission would be distributed beyond 5° from the pulsar as long as the pulsar is farther than 1 kpc from Earth. In our pulsar sample, four of them are located within 1 kpc and more than 80% of the total emission of pulsar halo population are contained within 5° from the pulsars. Therefore, it is safe to assume most of the energies of injected pairs are deposited in the Galactic plane, regardless of the transport model of pulsar halos.

APPENDIX B: PULSAR SAMPLES

Currently, the number of pulsars with characteristic age between 100 kyr and 10 Myr with known distance (including those inferred from dispersion measure) is 1164. Among them, 296 pulsars are within the ROI for AS γ (i.e., $25^\circ < l < 100^\circ$, $|b| < 5^\circ$) and 142 samples are

within the ROI for MILAGRO (i.e., $40^\circ < l < 100^\circ$, $|b| < 5^\circ$). After performing the mask procedure and the removal of PSR J1952 + 3252 as introduced in Sec. II A, 236 pulsar samples remained as potential sources contributing to the observed DGE for AS γ , and 217 pulsar samples remained for MILAGRO. The detailed information of these pulsars is listed in Table I.

Among all the samples, PSR J1952 + 3252 stands out for its high spin-down luminosity, short rotation period, and association with an SNR, as shown in Fig. 7. Other three pulsars of SNR associations have relatively slow rotation and low spin-down luminosity. The pulsar with the second highest spin-down luminosity and the second shortest period, PSR J1925 + 1720, does not have an SNR association. Because of the specificity, we speculate that PSR J1952 + 3252 might be much younger than its characteristic age and exclude it in our calculation.

TABLE I. Middle-aged pulsar samples selected in our calculation within $25^\circ < l < 100^\circ$, $|b| < 5^\circ$.

JName	l [$^\circ$]	b [$^\circ$]	P [s]	\dot{P} [s/s]	L_s [erg s $^{-1}$]	d [kpc]
J1820-0427	25.46	4.73	0.598082	6.33×10^{-15}	$1.17 \times 10^{+33}$	2.857
J1821-0331	26.39	4.98	0.902316	2.53×10^{-15}	$1.36 \times 10^{+32}$	7.556
J1829 + 0000	30.46	4.82	0.199147	5.25×10^{-16}	$2.62 \times 10^{+33}$	4.353
J1830-0131	29.16	3.99	0.152512	2.11×10^{-15}	$2.34 \times 10^{+33}$	3.502
J1832 + 0029	31.25	4.36	0.533918	1.55×10^{-15}	$4.03 \times 10^{+32}$	1.120
J1833-0209	28.92	3.09	0.291931	2.75×10^{-15}	$4.37 \times 10^{+33}$	13.360
J1833-0338	27.66	2.27	0.686733	4.16×10^{-14}	$5.07 \times 10^{+33}$	2.500
J1833-0559	25.51	1.32	0.483459	1.23×10^{-14}	$4.31 \times 10^{+33}$	6.827
J1834-0602	25.64	0.97	0.487914	1.83×10^{-15}	$6.21 \times 10^{+32}$	6.340
J1835-0349	27.68	1.86	0.841865	3.06×10^{-15}	$2.02 \times 10^{+32}$	5.510
J1835-0600	25.76	0.83	2.221787	8.43×10^{-15}	$3.03 \times 10^{+31}$	10.644
J1836-0436	27.17	1.13	0.354237	1.66×10^{-15}	$1.48 \times 10^{+33}$	4.358
J1836-0517	26.51	0.92	0.457245	1.30×10^{-15}	$5.38 \times 10^{+32}$	8.315
J1837-0045	30.67	2.75	0.617037	1.68×10^{-15}	$2.83 \times 10^{+32}$	3.145
J1837-0559	26.00	0.38	0.201064	3.31×10^{-15}	$1.61 \times 10^{+33}$	4.315
J1839-0141	30.01	1.97	0.933266	5.94×10^{-15}	$2.89 \times 10^{+32}$	6.074
J1839-0223	29.50	1.46	1.26679	4.76×10^{-15}	$9.25 \times 10^{+31}$	6.088
J1839-0321	28.60	1.10	0.238782	1.25×10^{-14}	$3.63 \times 10^{+33}$	7.852
J1839-0332	28.46	0.93	2.675682	4.76×10^{-15}	$9.81 \times 10^{+30}$	4.042
J1839-0402	28.02	0.73	0.52094	7.69×10^{-15}	$2.15 \times 10^{+33}$	4.231
J1839-0436	27.41	0.65	0.149461	8.1×10^{-16}	$9.57 \times 10^{+33}$	4.483
J1839-0459	27.15	0.32	0.585319	3.31×10^{-15}	$6.51 \times 10^{+32}$	3.945
J1840 + 0214	33.70	3.44	0.797478	8.29×10^{-15}	$6.46 \times 10^{+32}$	5.846
J1840-0445	27.49	0.20	0.422316	1.13×10^{-14}	$5.91 \times 10^{+33}$	4.557
J1840-0626	25.93	-0.46	1.893353	2.30×10^{-14}	$1.34 \times 10^{+32}$	5.727
J1841-0157	30.10	1.22	0.663321	1.81×10^{-14}	$2.45 \times 10^{+33}$	7.930
J1841-0425	27.82	0.28	0.186149	6.39×10^{-15}	$3.91 \times 10^{+33}$	4.399
J1841-0500	27.32	-0.03	0.912916	3.48×10^{-14}	$1.80 \times 10^{+33}$	4.969
J1842-0153	30.28	1.02	1.054228	6.72×10^{-15}	$2.26 \times 10^{+32}$	6.875
J1842 + 0257	34.56	3.34	3.088256	2.96×10^{-14}	$3.97 \times 10^{+31}$	4.990
J1842 + 0358	35.43	3.85	0.233326	8.11×10^{-16}	$2.52 \times 10^{+33}$	4.329
J1842-0415	28.09	0.11	0.526682	2.19×10^{-14}	$5.93 \times 10^{+33}$	3.605
J1843-0000	32.01	1.77	0.880334	7.77×10^{-15}	$4.50 \times 10^{+32}$	3.336

(Table continued)

TABLE I. (*Continued*)

JName	l [°]	b [°]	P [s]	\dot{P} [s/s]	L_s [erg s ⁻¹]	d [kpc]
J1843 + 0119	33.20	2.39	1.266998	3.76×10^{-15}	$7.29 \times 10^{+31}$	6.069
J1843-0137	30.54	1.09	0.669872	2.47×10^{-15}	$3.24 \times 10^{+32}$	7.662
J1843-0211	30.08	0.77	2.027524	1.44×10^{-14}	$6.84 \times 10^{+31}$	5.931
J1843-0408	28.37	-0.17	0.781934	2.39×10^{-15}	$1.97 \times 10^{+32}$	3.983
J1843-0510	27.39	-0.52	0.671614	3.89×10^{-15}	$5.07 \times 10^{+32}$	4.068
J1843-0702	25.74	-1.43	0.191615	2.14×10^{-15}	$1.20 \times 10^{+33}$	4.285
J1843-0744	25.09	-1.68	0.475393	1.33×10^{-14}	$4.89 \times 10^{+33}$	7.053
J1844-0030	31.71	1.27	0.641098	6.08×10^{-15}	$9.11 \times 10^{+32}$	10.411
J1844-0433	28.10	-0.55	0.991027	3.91×10^{-15}	$1.59 \times 10^{+32}$	3.074
J1844-0452	27.75	-0.58	0.269443	6.80×10^{-16}	$1.37 \times 10^{+33}$	5.684
J1844-0538	27.07	-0.94	0.255704	9.71×10^{-15}	$2.29 \times 10^{+33}$	5.404
J1845-0434	28.19	-0.78	0.486751	1.13×10^{-14}	$3.88 \times 10^{+33}$	4.093
J1845-0545	27.15	-1.34	1.092348	1.34×10^{-14}	$4.07 \times 10^{+32}$	5.471
J1845-0635	26.35	-1.60	0.340528	4.49×10^{-15}	$4.49 \times 10^{+33}$	9.407
J1845-0743	25.43	-2.30	0.104695	3.67×10^{-16}	$1.26 \times 10^{+33}$	7.113
J1846 + 0051	33.16	1.44	0.434373	1.12×10^{-14}	$5.41 \times 10^{+33}$	3.998
J1846-0749	25.39	-2.43	0.35011	1.26×10^{-15}	$1.16 \times 10^{+33}$	13.990
J1846-07492	25.37	-2.39	0.86138	5.19×10^{-15}	$3.20 \times 10^{+32}$	4.220
J1847-0402	28.88	-0.94	0.597809	5.17×10^{-14}	$9.55 \times 10^{+33}$	3.419
J1847-0438	28.37	-1.27	0.957991	1.09×10^{-14}	$4.91 \times 10^{+32}$	4.378
J1847-0605	27.05	-1.87	0.778164	4.65×10^{-15}	$3.89 \times 10^{+32}$	4.324
J1848-0055	31.80	0.17	0.274557	1.35×10^{-15}	$2.57 \times 10^{+33}$	7.408
J1848-0511	27.94	-1.66	1.637129	8.86×10^{-15}	$7.97 \times 10^{+31}$	8.799
J1848 + 0604	38.06	3.33	2.218603	3.74×10^{-15}	$1.35 \times 10^{+31}$	12.600
J1848 + 0647	38.70	3.65	0.505957	8.75×10^{-15}	$2.67 \times 10^{+33}$	1.128
J1849-0040	32.08	0.20	0.672481	1.11×10^{-14}	$1.45 \times 10^{+33}$	7.887
J1849 + 0106	33.74	0.84	1.832259	1.70×10^{-14}	$1.09 \times 10^{+32}$	4.581
J1849 + 0127	34.03	1.04	0.542155	2.80×10^{-14}	$6.93 \times 10^{+33}$	4.691
J1849-0317	29.83	-1.17	0.668408	2.20×10^{-14}	$2.91 \times 10^{+33}$	1.212
J1849 + 0409	36.37	2.42	0.761194	2.16×10^{-14}	$1.93 \times 10^{+33}$	1.974
J1849-0614	27.18	-2.47	0.953384	5.39×10^{-14}	$2.46 \times 10^{+33}$	3.504
J1849-0636	26.77	-2.50	1.451319	4.62×10^{-14}	$5.97 \times 10^{+32}$	3.849
J1850-0031	32.37	-0.04	0.734185	1.26×10^{-15}	$1.26 \times 10^{+32}$	6.502
J1851-0029	32.54	-0.34	0.518721	4.74×10^{-15}	$1.34 \times 10^{+33}$	5.453
J1851-0114	31.81	-0.53	0.953182	2.48×10^{-15}	$1.13 \times 10^{+32}$	5.214
J1851 + 0233	35.18	1.23	0.344018	2.18×10^{-15}	$2.12 \times 10^{+33}$	12.653
J1851 + 0241	35.31	1.25	4.491318	2.26×10^{-14}	$9.83 \times 10^{+30}$	11.117
J1851-0241	30.52	-1.19	0.435194	7.96×10^{-15}	$3.81 \times 10^{+33}$	7.922
J1851 + 0418	36.72	2.05	0.284697	1.09×10^{-15}	$1.86 \times 10^{+33}$	4.089
J1852-0118	31.87	-0.78	0.451473	1.76×10^{-15}	$7.54 \times 10^{+32}$	4.726
J1852-0127	31.71	-0.80	0.428979	5.15×10^{-15}	$2.57 \times 10^{+33}$	5.692
J1852-0635	27.22	-3.34	0.524157	1.46×10^{-14}	$4.01 \times 10^{+33}$	4.577
J1853 + 0056	34.02	-0.04	0.275578	2.14×10^{-14}	$4.03 \times 10^{+33}$	3.841
J1853 + 0427	37.17	1.51	1.320659	2.65×10^{-15}	$4.53 \times 10^{+31}$	15.719
J1853 + 0545	38.35	2.06	0.1264	6.12×10^{-16}	$1.20 \times 10^{+33}$	6.519
J1854 + 0306	35.99	0.83	4.55782	1.45×10^{-13}	$6.05 \times 10^{+31}$	4.498
J1854-0524	28.51	-3.24	0.544021	1.20×10^{-15}	$2.94 \times 10^{+32}$	5.014
J1855 + 0306	36.17	0.48	1.633566	7.00×10^{-15}	$6.34 \times 10^{+31}$	7.422
J1855 + 0307	36.17	0.53	0.845348	1.81×10^{-14}	$1.18 \times 10^{+33}$	5.940
J1855 + 0700	39.61	2.34	0.258685	7.52×10^{-16}	$1.71 \times 10^{+33}$	10.336
J1856 + 0102	34.43	-0.65	0.620217	1.22×10^{-15}	$2.02 \times 10^{+32}$	6.540
J1856-0526	28.64	-3.58	0.370483	1.70×10^{-15}	$1.32 \times 10^{+33}$	4.034

(Table continued)

TABLE I. (*Continued*)

JName	l [°]	b [°]	P [s]	\dot{P} [s/s]	L_s [erg s ⁻¹]	d [kpc]
J1857 + 0526	38.44	1.19	0.349951	6.93×10^{-15}	$6.38 \times 10^{+33}$	12.231
J1858 + 0346	37.08	0.18	0.256844	2.04×10^{-15}	$4.75 \times 10^{+33}$	5.490
J1859 + 0601	39.24	0.90	1.044313	2.55×10^{-14}	$8.84 \times 10^{+32}$	6.364
J1859 + 0603	39.27	0.93	0.508561	1.59×10^{-15}	$4.77 \times 10^{+32}$	9.003
J1900-0134	32.55	-2.72	1.832332	3.05×10^{-14}	$1.96 \times 10^{+32}$	4.854
J1900 + 0227	36.17	-0.93	0.374262	5.71×10^{-15}	$4.30 \times 10^{+33}$	4.515
J1900 + 0438	38.07	0.17	0.312314	3.23×10^{-15}	$4.19 \times 10^{+33}$	6.988
J1900 + 0634	39.81	0.99	0.389869	5.13×10^{-15}	$3.41 \times 10^{+33}$	8.595
J1901 + 0124	35.38	-1.68	0.318817	3.24×10^{-15}	$3.95 \times 10^{+33}$	6.597
J1901 + 0156	35.82	-1.37	0.288219	2.36×10^{-15}	$3.89 \times 10^{+33}$	3.229
J1901 + 0234	36.37	-1.05	0.88524	2.30×10^{-14}	$1.31 \times 10^{+33}$	7.523
J1901-0312	31.19	-3.65	0.355725	2.29×10^{-15}	$2.01 \times 10^{+33}$	3.778
J1901-0315	31.15	-3.67	0.801693	2.57×10^{-15}	$1.97 \times 10^{+32}$	8.445
J1901 + 0331	37.21	-0.64	0.65545	7.46×10^{-15}	$1.05 \times 10^{+33}$	7.000
J1901 + 0355	37.58	-0.44	0.554756	1.27×10^{-14}	$2.95 \times 10^{+33}$	6.685
J1901 + 0413	37.81	-0.23	2.66308	1.32×10^{-13}	$2.75 \times 10^{+32}$	5.342
J1902 + 0248	36.74	-1.25	1.223777	2.41×10^{-15}	$5.18 \times 10^{+31}$	5.990
J1902 + 0556	39.50	0.21	0.746577	1.29×10^{-14}	$1.22 \times 10^{+33}$	3.600
J1902 + 0615	39.81	0.34	0.673505	7.71×10^{-15}	$9.96 \times 10^{+32}$	7.000
J1903 + 0135	35.73	-1.96	0.729307	4.03×10^{-15}	$4.10 \times 10^{+32}$	3.300
J1903-0258	31.66	-4.04	0.301459	6.79×10^{-16}	$9.79 \times 10^{+32}$	4.069
J1903 + 0601	39.65	0.11	0.374117	1.92×10^{-14}	$1.45 \times 10^{+33}$	5.887
J1904-0150	32.83	-3.84	0.379387	8.90×10^{-16}	$6.43 \times 10^{+32}$	5.305
J1905-0056	33.69	-3.55	0.643183	3.06×10^{-15}	$4.54 \times 10^{+32}$	7.644
J1905 + 0600	39.84	-0.28	0.44121	1.11×10^{-15}	$5.11 \times 10^{+32}$	8.797
J1906 + 0414	38.48	-1.51	1.043362	1.15×10^{-14}	$3.98 \times 10^{+32}$	10.069
J1906 + 0509	39.29	-1.08	0.39759	5.22×10^{-15}	$3.28 \times 10^{+33}$	3.091
J1907 + 0249	37.31	-2.32	0.351879	1.14×10^{-15}	$1.03 \times 10^{+33}$	8.751
J1907 + 0345	38.08	-1.80	0.240153	8.22×10^{-15}	$2.34 \times 10^{+33}$	9.481
J1907 + 0534	39.72	-0.99	1.138403	3.15×10^{-15}	$8.43 \times 10^{+31}$	11.835
J1908 + 0500	39.29	-1.40	0.291021	2.59×10^{-15}	$4.14 \times 10^{+33}$	5.845
J1909 + 0007	35.12	-3.98	1.016948	5.52×10^{-15}	$2.07 \times 10^{+32}$	4.358
J1909 + 0254	37.60	-2.71	0.989831	5.53×10^{-15}	$2.25 \times 10^{+32}$	4.500
J1910 + 0358	38.61	-2.34	2.330263	4.47×10^{-15}	$1.39 \times 10^{+31}$	2.859
J1914 + 0219	37.63	-4.04	0.457527	1.02×10^{-15}	$4.20 \times 10^{+32}$	14.386
J1857 + 0809	40.84	2.45	0.502924	4.74×10^{-15}	$1.47 \times 10^{+33}$	13.138
J1901 + 0716	40.57	1.06	0.643999	2.29×10^{-15}	$3.38 \times 10^{+32}$	3.400
J1902 + 1141	44.54	2.98	0.40914	2.59×10^{-15}	$1.49 \times 10^{+33}$	13.888
J1903 + 0654	40.50	0.39	0.791232	1.06×10^{-14}	$8.44 \times 10^{+32}$	5.923
J1903 + 0912	42.52	1.49	0.166314	1.48×10^{-14}	$1.27 \times 10^{+35}$	11.845
J1903 + 0925	42.74	1.54	0.357155	3.69×10^{-14}	$3.20 \times 10^{+33}$	6.256
J1904 + 0738	41.18	0.68	0.208958	4.11×10^{-16}	$1.78 \times 10^{+33}$	6.154
J1904 + 0800	41.50	0.86	0.263345	1.73×10^{-14}	$3.74 \times 10^{+33}$	10.966
J1905 + 0616	40.07	-0.17	0.989706	1.35×10^{-13}	$5.51 \times 10^{+33}$	4.952
J1905 + 0709	40.94	0.06	0.64804	4.94×10^{-15}	$7.17 \times 10^{+32}$	4.980
J1905 + 0902	42.56	1.06	0.218253	3.5×10^{-15}	$1.33 \times 10^{+33}$	11.553
J1905 + 1034	43.92	1.76	1.72681	2.07×10^{-14}	$1.59 \times 10^{+32}$	6.910
J1906 + 0641	40.60	-0.30	0.267275	2.14×10^{-15}	$4.42 \times 10^{+33}$	7.000
J1906 + 0724	41.22	0.07	1.53649	3.00×10^{-15}	$3.26 \times 10^{+31}$	6.929
J1906 + 0746	41.60	0.15	0.144073	2.03×10^{-14}	$2.68 \times 10^{+35}$	7.400
J1907 + 0731	41.50	-0.21	0.363676	1.84×10^{-14}	$1.51 \times 10^{+33}$	4.994
J1907 + 1149	45.29	1.83	1.42016	1.60×10^{-13}	$2.20 \times 10^{+33}$	7.551

(Table continued)

TABLE I. (*Continued*)

JName	l [°]	b [°]	P [s]	\dot{P} [s/s]	L_s [erg s ⁻¹]	d [kpc]
J1907 + 1247	46.10	2.37	0.827097	1.95×10^{-15}	$1.36 \times 10^{+32}$	10.526
J1908 + 0734	41.59	-0.27	0.212353	8.25×10^{-16}	$3.40 \times 10^{+33}$	0.669
J1908 + 0909	42.97	0.49	0.336555	3.49×10^{-14}	$3.61 \times 10^{+33}$	8.906
J1909 + 1102	44.83	0.99	0.283642	2.64×10^{-15}	$4.57 \times 10^{+33}$	4.800
J1909 + 1205	45.78	1.47	1.229312	3.40×10^{-15}	$7.23 \times 10^{+31}$	10.130
J1910 + 0534	40.06	-1.67	0.452867	1.92×10^{-15}	$8.18 \times 10^{+32}$	21.255
J1910 + 0714	41.52	-0.87	2.712423	6.12×10^{-15}	$1.21 \times 10^{+31}$	3.679
J1910 + 0728	41.74	-0.77	0.325415	8.31×10^{-15}	$9.52 \times 10^{+33}$	6.233
J1910 + 1017	44.25	0.52	0.411159	5.42×10^{-15}	$3.08 \times 10^{+33}$	13.677
J1910 + 1231	46.21	1.59	1.441742	8.23×10^{-15}	$1.08 \times 10^{+32}$	8.139
J1911 + 1051	44.89	0.50	0.190873	1.22×10^{-14}	$6.91 \times 10^{+33}$	10.118
J1911 + 1301	46.79	1.54	1.010462	1.89×10^{-15}	$7.23 \times 10^{+31}$	11.653
J1912 + 2104	54.09	4.99	2.232969	1.02×10^{-14}	$3.61 \times 10^{+31}$	3.369
J1913 + 0657	41.64	-1.71	1.257181	2.83×10^{-15}	$5.62 \times 10^{+31}$	5.069
J1913 + 0832	42.98	-0.86	0.134409	4.57×10^{-15}	$7.43 \times 10^{+33}$	8.204
J1913 + 0904	43.50	-0.68	0.163246	1.76×10^{-14}	$1.60 \times 10^{+35}$	2.997
J1913 + 1330	47.42	1.38	0.923391	8.68×10^{-15}	$4.35 \times 10^{+32}$	6.179
J1914 + 1428	48.46	1.49	1.15952	2.18×10^{-15}	$5.52 \times 10^{+31}$	6.514
J1915 + 0639	41.66	-2.37	0.64414	1.84×10^{-15}	$2.72 \times 10^{+32}$	8.874
J1915 + 0738	42.47	-1.8	1.542704	3.31×10^{-15}	$3.55 \times 10^{+31}$	1.404
J1915 + 0838	43.34	-1.3	0.342777	1.57×10^{-15}	$1.54 \times 10^{+33}$	10.840
J1915 + 1009	44.71	-0.65	0.404552	1.53×10^{-14}	$9.10 \times 10^{+33}$	7.000
J1916 + 0748	42.77	-2.05	0.541752	1.07×10^{-14}	$2.66 \times 10^{+33}$	11.779
J1916 + 0844	43.54	-1.49	0.439995	2.90×10^{-15}	$1.34 \times 10^{+33}$	10.988
J1916 + 0852	43.67	-1.45	2.182746	1.31×10^{-14}	$4.97 \times 10^{+31}$	9.391
J1916 + 0951	44.56	-1.02	0.270254	2.52×10^{-15}	$5.04 \times 10^{+33}$	1.904
J1916 + 1225	46.81	0.23	0.227387	2.35×10^{-14}	$7.87 \times 10^{+33}$	6.486
J1916 + 1312	47.58	0.45	0.281845	3.66×10^{-15}	$6.45 \times 10^{+33}$	4.500
J1917 + 0834	43.58	-1.89	2.129665	1.75×10^{-14}	$7.15 \times 10^{+31}$	1.231
J1917 + 1353	48.26	0.62	0.194631	7.20×10^{-15}	$3.85 \times 10^{+33}$	5.882
J1917 + 2224	55.78	4.55	0.425897	2.86×10^{-15}	$1.46 \times 10^{+33}$	4.965
J1918 + 1311	47.76	0.06	0.856749	2.26×10^{-15}	$1.42 \times 10^{+32}$	6.187
J1918 + 1541	49.89	1.36	0.370883	2.54×10^{-15}	$1.97 \times 10^{+33}$	0.727
J1920 + 1040	45.78	-1.59	2.215802	6.48×10^{-15}	$2.35 \times 10^{+31}$	10.151
J1921 + 0812	43.71	-2.93	0.210648	5.36×10^{-15}	$2.27 \times 10^{+33}$	2.896
J1921 + 0921	44.73	-2.42	0.562302	9.58×10^{-15}	$2.13 \times 10^{+33}$	6.139
J1921 + 1544	50.35	0.61	0.143576	9.80×10^{-16}	$1.31 \times 10^{+33}$	9.038
J1921 + 1630	50.95	1.14	0.936448	2.23×10^{-14}	$1.07 \times 10^{+33}$	5.097
J1922 + 1733	52.08	1.23	0.236171	1.34×10^{-14}	$4.01 \times 10^{+33}$	5.360
J1922 + 2110	55.28	2.94	1.077924	8.18×10^{-15}	$2.58 \times 10^{+32}$	4.000
J1924 + 1631	51.40	0.32	2.935186	3.64×10^{-13}	$5.69 \times 10^{+32}$	10.183
J1924 + 1639	51.42	0.56	0.158043	2.56×10^{-15}	$2.56 \times 10^{+33}$	5.059
J1924 + 2040	55.02	2.33	0.23779	2.09×10^{-15}	$6.14 \times 10^{+33}$	5.951
J1925 + 1720	52.18	0.59	0.075659	1.05×10^{-14}	$9.54 \times 10^{+35}$	5.048
J1926 + 1648	51.86	0.06	0.579823	1.8×10^{-14}	$3.64 \times 10^{+33}$	6.000
J1926 + 2016	54.85	1.80	0.299072	3.50×10^{-15}	$5.17 \times 10^{+33}$	5.948
J1927 + 1856	53.81	0.94	0.298313	2.24×10^{-15}	$3.34 \times 10^{+33}$	3.100
J1928 + 1923	54.28	1.02	0.81733	6.35×10^{-15}	$4.59 \times 10^{+32}$	10.583
J1929 + 1357	49.63	-1.81	0.866927	3.66×10^{-15}	$2.22 \times 10^{+32}$	4.768
J1929 + 1955	54.88	1.02	0.257832	2.56×10^{-15}	$5.89 \times 10^{+33}$	6.603
J1929 + 2121	56.12	1.75	0.723599	2.14×10^{-15}	$2.23 \times 10^{+32}$	2.653
J1930 + 1316	49.12	-2.32	0.760032	3.66×10^{-15}	$3.29 \times 10^{+32}$	6.339

(Table continued)

TABLE I. (*Continued*)

JName	l [°]	b [°]	P [s]	\dot{P} [s/s]	L_s [erg s ⁻¹]	d [kpc]
J1931 + 1439	50.54	-2.01	1.779226	6.33×10^{-15}	$4.44 \times 10^{+31}$	6.123
J1931 + 1536	51.41	-1.60	0.314355	5.01×10^{-15}	$6.37 \times 10^{+33}$	4.011
J1932 + 1059	47.38	-3.88	0.226519	1.16×10^{-15}	$3.93 \times 10^{+33}$	0.310
J1932 + 2020	55.58	0.64	0.268217	4.22×10^{-15}	$8.63 \times 10^{+33}$	5.000
J1933 + 2421	59.48	2.39	0.81369	8.11×10^{-15}	$5.94 \times 10^{+32}$	4.639
J1935 + 1616	52.44	-2.09	0.358738	6.00×10^{-15}	$5.13 \times 10^{+33}$	3.700
J1935 + 1829	54.36	-1.0	0.843548	2.32×10^{-15}	$1.53 \times 10^{+32}$	8.616
J1936 + 1536	51.88	-2.46	0.967338	4.04×10^{-15}	$1.76 \times 10^{+32}$	4.624
J1936 + 2042	56.38	-0.07	1.390723	4.94×10^{-14}	$7.25 \times 10^{+32}$	4.999
J1937 + 1505	51.57	-2.98	2.872774	5.61×10^{-15}	$9.34 \times 10^{+30}$	6.450
J1937 + 2544	60.84	2.27	0.20098	6.43×10^{-16}	$3.13 \times 10^{+33}$	3.125
J1937 + 2950	64.50	4.12	1.657429	3.48×10^{-15}	$3.02 \times 10^{+31}$	7.477
J1938 + 2010	56.12	-0.67	0.687082	3.40×10^{-15}	$4.14 \times 10^{+32}$	8.812
J1938 + 2659	62.11	2.56	0.883332	3.23×10^{-15}	$1.85 \times 10^{+32}$	8.576
J1939 + 2449	60.17	1.36	0.645302	1.83×10^{-14}	$2.68 \times 10^{+33}$	7.115
J1940 + 2245	58.63	0.13	0.258912	1.27×10^{-14}	$2.89 \times 10^{+33}$	8.081
J1941 + 1341	50.80	-4.47	0.559084	1.24×10^{-15}	$2.80 \times 10^{+32}$	5.459
J1941 + 2525	61.04	1.26	2.306153	1.61×10^{-13}	$5.18 \times 10^{+32}$	11.168
J1946 + 2535	61.81	0.28	0.515167	5.64×10^{-15}	$1.63 \times 10^{+33}$	8.305
J1946 + 2611	62.32	0.60	0.43506	2.2×10^{-14}	$1.05 \times 10^{+33}$	7.555
J1947 + 1957	56.99	-2.66	0.157509	5.23×10^{-16}	$5.28 \times 10^{+33}$	6.767
J1948 + 2333	60.21	-1.04	0.528352	1.36×10^{-14}	$3.63 \times 10^{+33}$	8.048
J1948 + 2551	62.21	0.13	0.196627	9.02×10^{-15}	$4.69 \times 10^{+33}$	8.698
J1948 + 2819	64.37	1.31	0.932693	6.13×10^{-14}	$2.98 \times 10^{+33}$	11.042
J1950 + 3001	66.09	1.75	2.788918	1.49×10^{-13}	$2.71 \times 10^{+32}$	8.759
J1952 + 3021	66.53	1.65	1.665665	1.08×10^{-14}	$9.25 \times 10^{+31}$	7.485
J1954 + 2407	61.37	-1.87	0.193405	1.06×10^{-15}	$5.76 \times 10^{+33}$	4.176
J1958 + 3033	67.35	0.69	1.098581	6.46×10^{-15}	$1.92 \times 10^{+32}$	7.266
J2000 + 2920	66.55	-0.35	3.073783	3.74×10^{-14}	$5.09 \times 10^{+31}$	6.684
J2002 + 3217	69.26	0.88	0.696761	1.05×10^{-13}	$1.23 \times 10^{+33}$	6.458
J2004 + 3137	69.01	0.02	2.111265	7.46×10^{-14}	$3.13 \times 10^{+32}$	8.000
J2005 + 3552	72.71	2.14	0.307943	2.99×10^{-15}	$4.04 \times 10^{+33}$	14.652
J2006 + 3102	68.67	-0.53	0.163695	2.49×10^{-14}	$2.24 \times 10^{+35}$	6.035
J2007 + 3120	69.04	-0.54	0.608205	1.56×10^{-14}	$2.74 \times 10^{+33}$	6.906
J2008 + 2513	64.06	-4.11	0.589196	5.40×10^{-15}	$1.04 \times 10^{+33}$	4.030
J2010 + 3230	70.39	-0.50	1.442448	3.62×10^{-15}	$4.76 \times 10^{+31}$	13.034
J2011 + 3331	71.32	-0.05	0.931733	1.79×10^{-15}	$8.72 \times 10^{+31}$	8.603
J2013 + 3845	75.93	2.48	0.230194	8.85×10^{-15}	$2.86 \times 10^{+33}$	7.123
J2018 + 3431	73.04	-0.84	0.387664	1.84×10^{-15}	$1.24 \times 10^{+33}$	6.636
J2022 + 2854	68.86	-4.67	0.343402	1.89×10^{-15}	$1.85 \times 10^{+33}$	2.100
J2029 + 3744	76.90	-0.73	1.216805	1.23×10^{-14}	$2.70 \times 10^{+32}$	5.771
J2030 + 3641	76.12	-1.44	0.200129	6.50×10^{-15}	$3.20 \times 10^{+33}$	6.947
J2030 + 4415	82.34	2.88	0.22707	6.48×10^{-15}	$2.19 \times 10^{+33}$	0.720
J2037 + 3621	76.75	-2.84	0.618715	4.50×10^{-15}	$7.50 \times 10^{+32}$	4.851
J2047 + 5029	89.06	4.38	0.445945	4.18×10^{-15}	$1.86 \times 10^{+33}$	3.973
J2053 + 4718	87.21	1.62	4.910379	1.48×10^{-14}	$4.94 \times 10^{+30}$	8.901
J2150 + 5247	97.52	-0.92	0.332206	1.01×10^{-14}	$1.09 \times 10^{+33}$	3.610

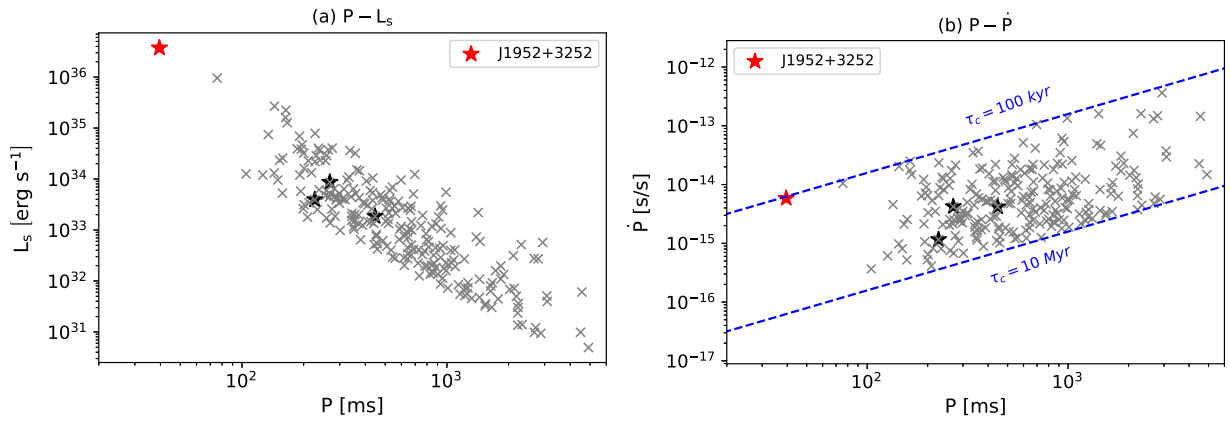


FIG. 7. Left: distributions of pulsars in the sample (Table I) including PSR J1952 + 3252 in the P - L_s plane. Stars (crosses) represent pulsars with (without) SNR association, where PSR J1952 + 3252 is marked as the red star. Right: same as the left panel but for the distribution in P - \dot{P} plane. The two dashed blue lines indicate the characteristic age of pulsars at 100 kyr and 10 Myr, respectively.

APPENDIX C: DISTANCE-DEPENDENT CORRECTION FACTOR

Yusifov and Küçük [45] suggested two categories of instrumental selection effects: one is the direction-dependent (mostly longitudinal) effect, which is related to the variation of noise from the sky, while the other is the distance-dependent effect because the flux of a pulsar is proportional to $1/d^2$. As the considered ROI ($25^\circ < l < 100^\circ$) is away from the Galactic center, the direction-dependent factor does not vary much in the ROI.

Thus, we only examine the influence of the distance-dependent selection effect. We follow Yusifov and Küçük [45] to take the distance-dependent correction factor $f_d = \exp(-c_0 d)$, where $c_0 = 0.362 \pm 0.017$ and d is the distance to the observer in unit of kpc. Then we weigh the contribution of each single pulsar halo to the DGE by the correction factor f_d , as we did for the beaming factor f_{beam} . Figure 8 shows the parameter constraints after considering the correction factor. The obtained upper limits of η_e are reduced by about an order of magnitude after the correction.

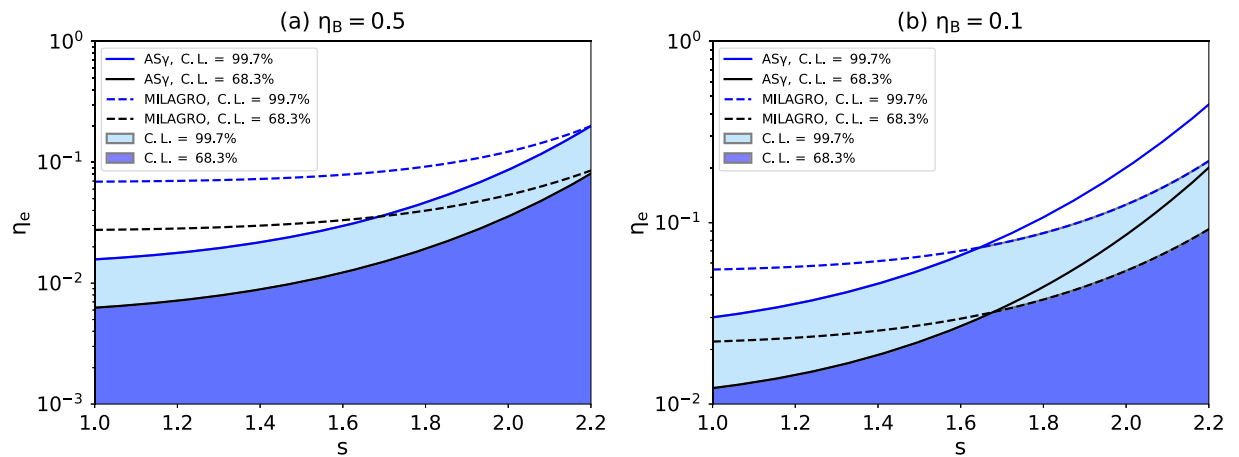


FIG. 8. Two-dimensional constraints between s and η_e after considering selection effect of pulsar detection. Other details are the same as in Fig. 4.

- [1] M. Ackermann, M. Ajello, W. B. Atwood, L. Baldini, J. Ballet, G. Barbiellini, D. Bastieri, K. Bechtol, R. Bellazzini, B. Berenji *et al.*, *Astrophys. J.* **750**, 3 (2012).
- [2] A. Neronov and D. Semikoz, *Astron. Astrophys.* **633**, A94 (2020).
- [3] R. Atkins, W. Benbow, D. Berley, E. Blaufuss, D. G. Coyne, T. De Young, B. L. Dingus, D. E. Dorfan, R. W. Ellsworth, L. Fleysher *et al.*, *Phys. Rev. Lett.* **95**, 251103 (2005).
- [4] B. Bartoli, P. Bernardini, X. J. Bi, P. Branchini, A. Budano, P. Camarri, Z. Cao, R. Cardarelli, S. Catalanotti, S. Z. Chen *et al.*, *Astrophys. J.* **806**, 20 (2015).
- [5] M. Amenomori, Y. W. Bao, X. J. Bi, D. Chen, T. L. Chen, W. Y. Chen, X. Chen, Y. Chen, S. W. Cirennima, Cui, L. K. Danzengluobu, Ding *et al.*, *Phys. Rev. Lett.* **126**, 141101 (2021).
- [6] T. Linden and B. J. Buckman, *Phys. Rev. Lett.* **120**, 121101 (2018).
- [7] R.-Y. Liu and X.-Y. Wang, *Astrophys. J. Lett.* **914**, L7 (2021).
- [8] K. Fang, J. S. Gallagher, and F. Halzen, *Astrophys. J.* **933**, 190 (2022).
- [9] V. Vecchiotti, G. Pagliaroli, and F. L. Villante, *Commun. Phys.* **5**, 161 (2022).
- [10] V. Vecchiotti, F. Zuccarini, F. L. Villante, and G. Pagliaroli, *Astrophys. J.* **928**, 19 (2022).
- [11] R. López-Coto, E. de Oña Wilhelmi, F. Aharonian, E. Amato, and J. Hinton, *Nat. Astron.* **6**, 199 (2022).
- [12] R.-Y. Liu, *Int. J. Mod. Phys. A* **37**, 2230011 (2022).
- [13] A. U. Abeysekara, A. Albert, R. Alfaro, C. Alvarez, J. D. Álvarez, R. Arceo, J. C. Arteaga-Velázquez, D. Avila Rojas, H. A. Ayala Solares, A. S. Barber *et al.*, *Science* **358**, 911 (2017).
- [14] F. Aharonian, Q. An, L. X. Axikegu, Bai, Y. X. Bai, Y. W. Bao, D. Bastieri, X. J. Bi, Y. J. Bi, H. Cai, J. T. Cai *et al.*, *Phys. Rev. Lett.* **126**, 241103 (2021).
- [15] R.-Y. Liu, H. Yan, and H. Zhang, *Phys. Rev. Lett.* **123**, 221103 (2019).
- [16] S. Recchia, M. Di Mauro, F. A. Aharonian, L. Orusa, F. Donato, S. Gabici, and S. Manconi, *Phys. Rev. D* **104**, 123017 (2021).
- [17] K. Yan, R.-Y. Liu, S. Z. Chen, and X.-Y. Wang, *Astrophys. J.* **935**, 65 (2022).
- [18] P. De La Torre Luque, O. Fornieri, and T. Linden, *Phys. Rev. D* **106**, 123033 (2022).
- [19] L.-Z. Bao, K. Fang, X.-J. Bi, and S.-H. Wang, *Astrophys. J.* **936**, 183 (2022).
- [20] R. Trotta, G. Jóhannesson, I. V. Moskalenko, T. A. Porter, R. Ruiz de Austri, and A. W. Strong, *Astrophys. J.* **729**, 106 (2011).
- [21] R. N. Manchester, G. B. Hobbs, A. Teoh, and M. Hobbs, *Astron. J.* **129**, 1993 (2005).
- [22] S. P. Wakely and D. Horan, in *International Cosmic Ray Conference*, International Cosmic Ray Conference Vol. 3 (2008), pp. 1341–1344.
- [23] D. Hooper and T. Linden, *Phys. Rev. D* **105**, 103013 (2022).
- [24] W. Bednarek and M. Bartosik, *Astron. Astrophys.* **405**, 689 (2003).
- [25] D. Khangulyan, F. A. Aharonian, and S. R. Kelner, *Astrophys. J.* **783**, 100 (2014).
- [26] M. Fouka and S. Ouichaoui, *Res. Astron. Astrophys.* **13**, 680 (2013).
- [27] T. M. Tauris and R. N. Manchester, *Mon. Not. R. Astron. Soc.* **298**, 625 (1998).
- [28] A. M. Atoyan and F. A. Aharonian, *Mon. Not. R. Astron. Soc.* **278**, 525 (1996).
- [29] R. Kothes, W. Reich, and B. Uyaniker, *Astrophys. J.* **638**, 225 (2006).
- [30] J. D. Gelfand, P. O. Slane, and W. Zhang, *Astrophys. J.* **703**, 2051 (2009).
- [31] J. A. Hinton, S. Funk, R. D. Parsons, and S. Ohm, *Astrophys. J. Lett.* **743**, L7 (2011).
- [32] X. Tang and R. A. Chevalier, *Astrophys. J.* **752**, 83 (2012).
- [33] D. F. Torres, A. Cillis, J. Martín, and E. de Oña Wilhelmi, *J. High Energy Astrophys.* **1**, 31 (2014).
- [34] D. Khangulyan, M. Arakawa, and F. Aharonian, *Mon. Not. R. Astron. Soc.* **491**, 3217 (2020).
- [35] X.-H. Liang, C.-M. Li, Q.-Z. Wu, J.-S. Pan, and R.-Y. Liu, *Universe* **8**, 547 (2022).
- [36] P. Lipari and S. Vernetto, *Phys. Rev. D* **98**, 043003 (2018).
- [37] M. Di Mauro, S. Manconi, and F. Donato, *Phys. Rev. D* **100**, 123015 (2019).
- [38] X. Tang and T. Piran, *Mon. Not. R. Astron. Soc.* **484**, 3491 (2019).
- [39] O. C. de Jager and A. K. Harding, *Astrophys. J.* **396**, 161 (1992).
- [40] E. Amato and B. Olmi, *Universe* **7**, 448 (2021).
- [41] E. de Oña Wilhelmi, R. López-Coto, E. Amato, and F. Aharonian, *Astrophys. J. Lett.* **930**, L2 (2022).
- [42] G. Jóhannesson, T. A. Porter, and I. V. Moskalenko, *Astrophys. J.* **879**, 91 (2019).
- [43] P. Martin, A. Marcowith, and L. Tibaldo, *Astron. Astrophys.* **665**, A132 (2022).
- [44] P. M. Saz Parkinson, M. Dormody, M. Ziegler, P. S. Ray, A. A. Abdo, J. Ballet, M. G. Baring, A. Belfiore, T. H. Burnett, G. A. Caliandro *et al.*, *Astrophys. J.* **725**, 571 (2010).
- [45] I. Yusifov and I. Küçük, *Astron. Astrophys.* **422**, 545 (2004).
- [46] F. Acero, M. Ackermann, M. Ajello, A. Albert, L. Baldini, J. Ballet, G. Barbiellini, D. Bastieri, R. Bellazzini, E. Bissaldi *et al.*, *Astrophys. J. Suppl. Ser.* **223**, 26 (2016).
- [47] R. Yang, F. Aharonian, and C. Evoli, *Phys. Rev. D* **93**, 123007 (2016).
- [48] K. Fang, X.-J. Bi, and P.-F. Yin, *Astrophys. J.* **884**, 124 (2019).
- [49] S. Manconi, M. Di Mauro, and F. Donato, *Phys. Rev. D* **102**, 023015 (2020).